Title

An investigation of how specimen dimensions affect biaxial mechanical characterizations with CellScale BioTester and constitutive modeling of porcine tricuspid valve leaflets.

Authors

Laurence, Devin

Wang, Shuodao

Xiao, Rui

et al.

Publication Date

2023-11-01

DOI

10.1016/j.jbiomech.2023.111829

Peer reviewed

HHS Public Access

Author manuscript

J Biomech. Author manuscript; available in PMC 2024 November 01.

Published in final edited form as:

J Biomech. 2023 November ; 160: 111829. doi:10.1016/j.jbiomech.2023.111829.

An investigation of how specimen dimensions affect biaxial mechanical characterizations with CellScale BioTester and constitutive modeling of porcine tricuspid valve leaflets

Devin W. Laurence[a,*], **Shuodao Wang**[b], **Rui Xiao**[c], **Jin Qian**[c], **Arshid Mir**[d], **Harold M. Burkhart**[e], **Gerhard A. Holzapfel**[f,g], **Chung-Hao Lee**[a,h,i,**]

[a]Biomechanics and Biomaterials Design Laboratory, The University of Oklahoma, USA

[b]School of Mechanical and Aerospace Engineering, Oklahoma State University, USA

[c]Department of Engineering Mechanics, Key Laboratory of Soft Machines and Smart Devices of Zhejiang Province, Zhejiang University, Hangzhou 310027, China

[d]Department of Pediatrics, University of Oklahoma Health Sciences Center, USA

[e]Department of Surgery, University of Oklahoma Health Sciences Center, USA

[f]Institute of Biomechanics, Graz University of Technology, Austria

[g]Department of Structural Engineering, Norwegian University of Science and Technology, Norway

[h]Institute for Biomedical Engineering, Science and Technology, The University of Oklahoma, USA

[i]Department of Bioengineering, The University of California, Riverside, USA

Abstract

Biaxial mechanical characterizations are the accepted approach to determine the mechanical behavior of many biological soft tissues. Although several computational and experimental studies have examined how experimental factors (e.g., clamped vs. suture mounting) affect the acquired mechanical behavior, little is known about the role of specimen dimensions in data acquisition and subsequent modeling. We combined our established mechanical characterization framework with an iterative size-reduction protocol to test the hypothesis that specimen dimensions affect the observed mechanical behavior of biaxial characterizations. Our findings indicated that there

**Corresponding author. Chung-Hao Lee, Ph.D., Associate Professor, School of Aerospace and Mechanical Engineering, The University of Oklahoma, 865 Asp Ave., Felgar Hall 219C, Norman, OK 73019, USA, ch.lee@ou.edu, Tel: 405-325-4842.
*Division of Pediatric Cardiology, Children's Hospital of Philadelphia, USA

Conflict of Interest. The authors of this paper have no financial or personal relationships with other people or organizations that could inappropriately influence (bias) our work.

Declarations of Interest Statement

We, the authors of "*An investigation of how specimen dimensions affect biaxial mechanical characterizations with CellScale BioTester and constitutive modeling of porcine tricuspid valve leaflets*", attest that we hold no financial or personal relationships with other people or organizations that could inappropriately influence or bias our work.

We hereby also declare that all authors were fully involved in the study and preparation of the manuscript and the material within has not been and will not be submitted for publication elsewhere.

were non-significant differences in the peak equibiaxial stretches of tricuspid valve leaflets across four specimen dimensions ranging from 4.5 × 4.5 mm to 9 × 9 mm. Further analyses revealed that there were detectable significant differences in the low-tensile modulus of the circumferential tissue direction. These differences resulted in significantly different constitutive model parameters for the Tong-Fung model between different specimen dimensions of the posterior and septal leaflets. Overall, our findings demonstrate that specimen dimensions play an important role in experimental characterizations, but not necessarily in constitutive modeling of soft tissue mechanical behavior during biaxial testing with the commercial CellScale BioTester.

Keywords

biaxial tensile testing; heart valve leaflet; specimen dimension; constitutive modeling

1. Introduction

Finite element simulations of heart valve function require the detailed descriptions of how the tissues respond to applied loading (Sacks et al. (2019)). These mechanical behaviors are often derived from experimental characterizations, including uniaxial and biaxial tensile tests (Sacks (2000)). Although these methods have been widely accepted as the standard approaches to determine the mechanical behavior of soft tissue, inconsistencies in published protocols may confuse comparisons and the use of the data in *in silico* simulations.

Inspired by the seminal work of Nielsen et al. (1991), early studies focused on refining experimental protocols using finite element models that emulated the testing apparatus. For example, Sun et al. (2005) explored how different attachment methods (e.g., clamp or sutures) or specimen shapes (square vs. cruciform) influenced the homogeneity of the predicted tissue strains and stresses. Eilaghi et al. (2009) later expanded this work by exploring how the distribution of attachment points altered the experimental results. The authors noted that non-equibiaxial protocols were particularly influenced by the attachment properties. Jacobs et al. (2013) then used a refined finite element analysis to determine a correction factor that could account for the stress shielding and other boundary loading effects. This approach and the resulting metrics were later questioned and expanded by Nolan and McGarry (2016). Recent computational investigations have attempted to compare the numerical predictions with experimental findings (Avanzini and Battini (2016)) or to investigate emerging commercial testing platforms (Fehervary et al. (2016)).

Benchtop studies have also advanced our knowledge on how experimental factors influence biaxial tensile characterizations of heart valve leaflets. For example, Jett et al. (2018) showed that atrioventricular heart valve leaflets become more compliant in the radial direction with increasing tissue temperature. Later, Salinas et al. (2019) further demonstrated that testing media osmolarity was also crucial to acquiring accurate mechanical behaviors with non-physiological deionized water, resulting in reduced tissue extensibility. Other studies by Duginski et al. (2020) and Salinas et al. (2020) explored how freezer storage may alter the observed mechanical behavior and found that temporary freezer storage between −14°C and −80°C did not significantly alter the mechanical behavior of heart valve

leaflets. Recently there has also been interest in understanding the appropriate choice of the stress-free reference configuration (Laurence et al. (2022)) and the refined strain fields via dense speckle patterning (Sugerman et al. (2023)) or polarized light techniques (Dover et al. (2022)). Collectively, these experimental studies provide guidance for the development of frameworks and protocols to characterize the mechanical behavior of heart valve leaflets.

An area that still needs to be explored, particularly in the field of experimental tissue biomechanics, is how specimen dimensions influence the observed biomechanical behavior. We hypothesize that the specimen dimensions influence the observed mechanical behaviors as there is ample evidence that the insertion properties alter the homogeneity of the quantified tissue stress and strain fields. This would also lead to erroneous comparisons between studies with different specimen dimensions, as well as inaccurate estimates of the constitutive parameters and their use in subsequent *in silico* predictions.

Therefore, the aim of this work is to test this hypothesis and to quantify how specimen dimensions affect the mechanical behavior, mechanical properties and derived constitutive model parameters of tricuspid heart valve leaflets – our tissue application of choice. We achieve this by using our established biaxial mechanical characterization technique with an iterative reduction in specimen dimensions. The resulting mechanical behavior is analyzed to determine typical biomechanical properties (e.g., low- and high-tensile moduli). Furthermore, we fit the experimental data to three typical strain–energy functions to understand whether the dimension differences alter the constitutive behavior used in numerical simulations of heart valve function.

2. Methods

2.1. Tissue Acquisition and Preparation

Adult porcine hearts (n = 8, 80–140kg, 1–1.5 years of age) were obtained from a USDA-approved abattoir (Country Home Meats Company, Edmond, OK) and shipped to our laboratory. The hearts were cleaned to remove excess blood and the whole organ was immediately stored in a freezer at −14°C. The frozen hearts were thawed in a water bath at room temperature within a week, and the three TV leaflets were dissected using our established technique (Jett et al. (2018); Ross et al. (2019a)). All three dissected TV leaflets (n = 8 per leaflet), i.e., anterior leaflet (TVAL), posterior leaflet (TVPL), and septal leaflet (TVSL), were then temporarily stored in the freezer pending experimental characterization within 1–2days. This temporary frozen storage is supported by our previous investigation which found that short-term frozen storage of atrioventricular valve leaflets had negligible effects on the characterized mechanical properties (Duginski et al. (2020)).

In preparation for biaxial mechanical testing, the excised leaflet was thawed in phosphate-buffered saline (PBS). Then a 13×13 mm specimen was cut from the central region of each TV leaflet (Fig. 1(a)), and the upper right corner of the specimen was marked with a surgical pen for orientation. The average thickness of the tissue was determined from three separate measurements across the specimen with a digital caliper (Westward 1AAU4, 0.01 mm resolution). The tissue was next mounted on a BioTester (CellScale, Canada) using BioRakes to delineate an effective test region of 9 × 9 mm (Fig. 1(b)). Then four

glass beads (300–500 μm) were glued in a square configuration within the central one-third area of the effective test region (i.e., central 3 × 3 mm) for subsequent calculations of tissue deformations/strains using digital image correlation (DIC). Once the glass beads were attached to the tissue surface, the specimen was immersed in a 37°C PBS bath (Jett et al. (2020)).

2.2. Biaxial Mechanical Characterization

For biaxial tests, the target peak force f^{target} for the TV leaflet specimen was determined using the approximate maximum physiological stress P^{target} of 115 kPa according to previous literature (Jett et al. (2018); Khoiy and Amini (2016)), the initial effective edge length L_0 of the tissue and the undeformed thickness t_0: $f^{\text{target}} = P^{\text{target}} L_0 t_0$. The leaflet was first subjected to 10 cycles of force-controlled equibiaxial preconditioning to ensure repeatable mechanical behaviors. The post-preconditioned configuration was recorded for later analyses. Next, the tissue was returned to its initial mounted configuration and the functionality of the BioTester was used to determine the biaxial displacements associated with the varying ratios $f_{\text{circ}}^{\max} : f_{\text{rad}}^{\max} = 1:1, 1:0.667, 1:0.333, 0.667:1, 0.333:1$. The specimen was then allowed to rest at the mounted configuration for 3min. Finally, the tissue underwent biaxial mechanical characterization that included three loading/unloading cycles for each of the above-mentioned force ratios (i.e., protocols) at a loading rate of 1.31 N/min to emulate the quasi-static loading condition.

During the biaxial test, images were taken at 1280 × 960 resolution using the charge-couple device (CCD) camera and the load cell forces and tine displacements at 15 Hz. Data from the last loading cycle was used in the stress/strain analysis and constitutive modeling discussed in Section 2.4.

2.3. Iterative Approach to Determine the the Effect of Specimen Dimensions

In order to investigate the effect of the specimen sizes on the characterized mechanical behavior, a sequential test procedure was carried out (Fig. 1(b)). Immediately after mechanical characterization of the 9 × 9 mm effective test region, the specimen removed from the BioTester and the BioRake holes were used as guidelines to procure a smaller specimen of 9 × 9 mm. The 9 × 9 mm specimen was then mounted to the BioTester with the second effective test region of 7.5 × 7.5 mm to repeat the mechanical characterization procedure described in Section 2.2. This iterative process was repeated for the 7.5 × 7.5 mm and 6 × 6 mm specimen sizes, resulting in the characterization of a total of four effective test regions (9 × 9 mm, 7.5 × 7.5 mm, 6 × 6 mm, and 4.5 × 4.5 mm) referred to in this study. Where possible, the original glass beads from the first specimen size were retained throughout the iterative procedure. However, it was sometimes necessary to swap out the glass beads for the smallest dimensions to keep the position of the fiducial markers within the central one-third of the specimen and allow for a homogeneous strain calculation.

2.4. Calculations of Tissue Stretches, Stresses, and Other Derived Mechanics Metrics

The time-dependent fiducial marker positions were determined using the DIC functionality of the CellScale LabJoy software. The two-dimensional in-plane deformation gradient was

calculated using a four-node bilinear finite element and the marker displacements (Sacks (2000)), i.e.,

$$[\mathbf{F}] = [\mathbf{F}(\mathbf{X}, t)] = [\mathbf{I}] + \begin{bmatrix} \sum_{I=1}^{4} B_{XI} u_I(t) & \sum_{I=1}^{4} B_{YI} u_I(t) \\ \sum_{I=1}^{4} B_{XI} v_I(t) & \sum_{I=1}^{4} B_{YI} v_I(t) \end{bmatrix}. \quad (1)$$

Here $\mathbf{I}$ is the second-order identity tensor, B_{XI} and B_{YI} are the shape function derivatives of the marker I and $u_I(t)$ and $v_I(t)$ are the time-varying X and Y-displacements of the marker I with respect to the stress-free mounted configuration. The tissue stretches λ_{circ} and λ_{rad} were calculated as the square roots of the principal values of the right-Cauchy tensor $\mathbf{C} = \mathbf{F}^T\mathbf{F}$ (Holzapfel (2000)), and the preconditioning stretches λ_{circ}^{PC} and λ_{rad}^{PC} were determined after preconditioning using the configuration recorded in Section 2.3.

Remark 1: Note that the tine-based testing scheme minimizes shear deformations of the tissue in contrast to existing suture-based methods in the literature. Therefore, we have assumed negligible shear deformations in the calculated deformation gradient, Eq. (1), which is consistent with the study of Narang et al. (2021), which demonstrated minimal *in vivo* shear deformations in the central region of the heart valve leaflets.

The first Piola-Kirchhoff stresses P_{circ} and P_{rad} were determined as

$$[\mathbf{P}] = \mathrm{diag}[P_{circ}, P_{rad}] = \frac{1}{t_0 L_0}\mathrm{diag}[f_{circ}, f_{rad}], \quad (2)$$

where f_{circ} and f_{rad} are the forces measured in the circumferential and radial directions of the tissue, respectively.

The resulting stress-stretch curves were further analyzed to determine relevant engineering mechanics metrics, including the low-tensile moduli E_{circ}^{LT} and E_{rad}^{LT} using the experimental data < 10 kPa, the high-tensile moduli E_{circ}^{HT} and E_{rad}^{HT} using the last 5 data points of the loading curve (Fig. 1(c)), and the anisotropy index AI (May-Newman and Yin (1995); Pham et al. (2017); Wells et al. (2012)), calculated as the ratio of radial stretch to circumferential stretch under equibiaxial loading, i.e., $\lambda_{rad}/\lambda_{circ}$.

2.5. Constitutive Modeling

Furthermore, we examined the influence of the specimen dimensions on the determined constitutive model parameters for each leaflet ($n = 8$). Instead of performing a model fit to average experimental data (e.g., Khoiy et al. (2018)), we wanted to test the null hypothesis that *specimen dimensions do not change specimen-specific constitutive model parameters*. To test this, data from the equibiaxial loading protocol (P_{circ}:P_{rad} = 1:1) for all four effective test sizes were fit with three widely used constitutive models of heart valves and artery

tissues. Note that only the equibiaxial configuration was considered to avoid complications when fitting with multiple protocols and to isolate the effect of specimen dimensions on the optimal model parameters.

The first constitutive model is the Lee-Sacks constitutive model typically used for heart valve leaflets (Lee et al. (2014)), i.e.,

$$\Psi_{\mathrm{LS}} = C_{10}(I_1 - 3) + \frac{c_1}{2}\left\{\delta \exp\left[c_2(I_1 - 3)^2\right] + (1 - \delta)\exp\left[c_3(I_4 - 1)^2\right] - 1\right\}, \tag{3}$$

in which Ψ_{LS} is the strain–energy function, C_{10}, c_0, c_1, c_2 and c_3 are the model parameters to be determined, $I_1 = \mathrm{tr}\mathbf{C}$ is the first invariant of $\mathbf{C}$, $I_4 = \mathbf{N} \cdot (\mathbf{CN})$ is the fourth pseudo-invariant of $\mathbf{N}$ and $\mathbf{C}$, $[\mathrm{N}] = [\cos\theta, \sin\theta, 0]^{\mathrm{T}}$ denotes the matrix form of the unit vector $\mathbf{N}$, which describes the collagen fiber orientation with the angle θ, while $\delta \in [0, 1]$ describes the material anisotropy.

The second model considered is the phenomenological constitutive model for soft biological tissues proposed by Tong and Fung (1976), i.e.,

$$\Psi_{\mathrm{TF}} = C_{10}(I_1 - 3) + \frac{c}{2}\left[\exp\left(a_1 E_{\mathrm{circ}}^2 + a_2 E_{\mathrm{rad}}^2 + a_3 E_{\mathrm{circ}} E_{\mathrm{rad}}\right) - 1\right], \tag{4}$$

where C_{10}, c, a_1, a_2, and a_3 are the model parameters and E_{circ} and E_{rad} are the circumferential and radial Green-Lagrange strains, respectively.

Remark 2: Although this model has certain shortcomings, e.g., ignoring shear strains, Narang et al. (2021) showed negligible *in vivo* shear deformations in the central belly region of the leaflet, which was the focus of this work.

The final constitutive model was proposed by Gasser et al. (2006), the GOH model, i.e.,

$$\Psi_{\mathrm{GOH}} = C_{10}(I_1 - 3) + \frac{k_1}{2k_2}\left(\exp\left\{k_2\left[\kappa(I_1 - 3) + (1 - 3\kappa)(I_4 - 1)\right]^2\right\} - 1\right). \tag{5}$$

Herein, C_{10}, k_1, k_2, and κ are the model parameters, while the parameter $\kappa \in [0, 1/3]$ describes the collagen fiber dispersion.

An internal differential evolution optimization (DEO) algorithm was employed to estimate the material model parameters in Eqs. (3)–(5) by nonlinear least-squares regression (Yu et al. (2014)). For all three constitutive models, it was assumed that $C_{10} = 5$ kPa to reduce the number of parameters to be estimated and to ensure realistic and consistent low-stress behavior. Briefly, n_{pop} uniformly distributed sets of material parameters were generated, and the residual r was computed for each parameter set j. Thus,

$$r_j = \frac{1}{n_{\text{data}}}\left[\sum_{i=1}^{n_{\text{data}}}\left(S_{\text{circ}}^{\text{exp},i} - S_{\text{circ},j}^{\text{model},i}\right)^2 + \left(S_{\text{rad}}^{\text{exp},i} - S_{\text{rad},j}^{\text{model},i}\right)^2\right]^{1/2}, \tag{6}$$

where n_{ndata} denotes the number of experimental data points, S_{circ} and S_{rad} are the circumferential and radial second Piola-Kirchhoff stresses, respectively, and the superscript denotes either the experimental data or the model predictions. The n_{pop} residuals and their Euclidian distances to the best parameter set were used with the two-step DEO algorithm to iteratively update the parameter sets until the residual threshold was reached (max $r_j < 5 \times 10^{-7}$), or the change in the residual was minimal ($< 1 \times 10^{-7}$) for three consecutive iterations.

2.6. Statistical Analyses

Visualization of the data in MATLAB using quantile-quantile (Q-Q) plots showed the data were not normally distributed (not shown here). Therefore, two-factor comparisons (size vs. leaflets) were performed using the non-parametric aligned rank transform in R version R-4.2.2 (Wobbrock et al. (2011)). Comparisons were performed where $p < 0.05$ was considered statistically significant.

3. Results

3.1. Mechanical Behavior with Equibiaxial Tension

The TV leaflets showed nonlinear, anisotropic mechanical behavior under equibiaxial loading for all four specimen sizes, as shown in Fig. 2. Detailed comparisons of the peak stretches are provided in Fig. 3. Results for other biaxial tension protocols are given in Appendix A.

As expected, the circumferential directions of the leaflets were consistently stiffer than the radial directions due to collagen fiber reinforcement along the circumferential direction. For the circumferential direction, we observed stiffer stretches between the smallest (4.5×4.5mm) and largest (9×9 mm) specimen dimensions for the TVPL (1.28 vs. 1.50) and TVSL (1.29 vs. 1.41). Specimen dimensions had minimal effects on the radial tissue stretches between the smallest and largest specimen dimensions of TVPL (1.57 vs. 1.58) and TVSL (1.57 vs. 1.57). Interestingly, the TVAL had an opposite trend for the circumferential stretches (1.38 vs. 1.35) and the differences in the radial stretches (1.56 vs. 1.37) were more apparent.

3.2. Preconditioning Stretches

The quantified stretches after the preconditioning step ($\lambda_{\text{circ}}^{\text{PC}}$ and $\lambda_{\text{rad}}^{\text{PC}}$) are presented in Fig. 4. For both TVPL and TVSL in the circumferential (1.06–1.08 vs.1.14–1.17) and radial (1.29–1.34 vs.1.34–1.41) directions, we consistently observed smaller preconditioning stretches at the smallest specimen size (4.5×4.5mm) than the largest specimen size (9×9 mm). The TVAL, on the other hand, exhibited opposite trends with larger preconditioning stretches at

the smallest specimen dimensions (1.22–1.36) compared to the largest specimen dimensions (1.12–1.21). Significant differences were only found between leaflets for λ_{circ}^{PC} ($p = 0.03$).

3.3. Derived Mechanics-Related Metrics

The quantified low-tensile moduli E_{circ}^{LT} and E_{rad}^{LT}, high-tensile moduli E_{circ}^{HT} and E_{rad}^{HT} and anisotropy indices AI are given in Figs. 5–6 and Fig. 3, respectively.

We find that the circumferential low-tensile moduli E_{circ}^{LT} increased with smaller specimen dimensions for the TVPL (60.10 kPa vs. 19.51 kPa) and TVSL (37.1 kPa vs. 28.6 kPa), where the radial low-tensile moduli E_{rad}^{LT} remained consistent. These differences were significant between specimen sizes ($p = 0.01$). On the other hand, the circumferential and radial high-tensile moduli decreased with smaller specimen sizes for TVAL (1655.5–2583.6kPa vs.2806.9–3239.4kPa) and TVPL (1176.2–2692.9kPa vs.1753.3–2702.6), but increased with smaller specimen sizes for the TVSL (2645.5–4650.5kPa vs.2312.1–2878.4kPa). Significant differences were only found between leaflets ($p < 0.05$) and not between specimen dimensions ($p > 0.15$). Finally, the AI remained without significant differences at smaller specimen dimensions for TVAL (1.09 vs.1.12) and TVSL (1.14 vs.1.22) but increased for TVPL (1.19 vs.1.02).

3.4. Constitutive Modeling

The parameters for the Lee-Sacks constitutive model, i.e., Eq. (3), the Tong-Fung constitutive model, i.e., Eq. (4), and the GOH constitutive model, i.e., Eq. (5) are summarized in Tables 1–3. Interestingly, there was only one statistically significant difference for the Tong-Fung constitutive model parameter (c) between leaflets ($p < 0.01$) and specimen sizes ($p < 0.01$). When considering the interactions between these effects, the only significant comparison was between TVSL Size #2 ($c = 0.04$kPa) and the TVPL Size #4 ($c = 0.86$kPa). Therefore, the specimen dimensions do not have a significant effect on the derived constitutive model parameters for a given TV leaflet.

4. Discussion

4.1. Overall Findings

In this study, we performed biaxial tensile tests on TV leaflets to understand how specimen dimensions affect mechanical behavior, mechanical properties, and estimated constitutive model parameters. Our results demonstrated that reducing specimen size resulted in a slightly stiffer circumferential behavior and a slightly more compliant radial behavior. However, none of these differences were considered significant from the standpoint of statistical analysis. Further comparison of the derived mechanical properties illustrated a slight increase in low-tensile stiffness, a decrease in high-tensile stiffness, and an increase in AI with decreasing specimen dimensions, with the exception of TVSL. We detected one significant difference in the Tong-Func constitutive model stiffness c between two specimen sizes of the TVPL and TVSL.

4.2. Comparisons with Existing Literature

Although, to our knowledge, this is the first *experimental* study exploring how specimen dimensions affect biaxial mechanical characterization and constitutive modeling, some have attempted to study this feature *numerically*. Most notably, Fehervary et al. (2016) used finite element simulations of planar biaxial testing to understand how certain test factors affected the strain homogeneity within the fiducial markers and the accuracy of the constitutive model behavior. Through their *correction factor metric*, they observed that the predicted stresses increased (i.e., stiffer tissue) as the fiducial markers got closer to the tine insertions. The experimental findings in this work generally support this observation, with the exception of the TVSL, which was slightly more deformable with smaller sample dimensions. Another study by Eilaghi et al. (2009) underlined the importance of the insertion point distribution along the effective test region. In this study, we did not attempt to test this factor experimentally, however we used different sets of tines for each specimen edge length. Therefore, our data presented here may be useful for further investigations along this path.

Recent advances in polarized spatial frequency domain imaging have enabled the simultaneous acquisition of collagen fiber architectural properties and tissue strains (Dover et al. (2022)). In their work, Dover et al. (2022) assessed how the size of the region of interest affects strain homogeneity and analyses of tissue mechanical properties. They found that regions farther away from the boundary insertion points exhibited stiffer circumferential behavior and more compliant radial behavior (i.e., the strains are only homogeneous within the central 80% of the specimen dimension).

Our results from iterative biaxial mechanical characterization reflect this result and underscores the importance of specimen dimensions and defining an appropriate region of interest.

4.3. Implications of Our Findings

Our results have significant implications for existing mechanical studies using iterative experimental protocols. For example, our group used iterative enzyme-based approaches to characterize how glycosaminoglycans, collagen, and elastin contribute to the TV leaflet mechanical behavior (Ross et al. (2021, 2019b)). Control tissues were larger than enzyme-treated tissues in these studies to ensure that previous tine insertion holes did not affect the biomechanical perfomance. However, as our present study indicates, this reduction in specimen size results in higher circumferential stretches and lower radial stretches for the enzyme-treated specimens, which may result in misleading comparisons between the treated and control groups.

Beyond the scope of individual experimental investigations, our results also suggest that specimen size must be considered when comparing the mechanical behavior within the existing literature. Researchers typically do not control for specimen size in their studies (Table 4), which means direct comparisons can be problematic due to the specimen size effect presented herein. Additionally, studies can use different stress-free reference configurations such as the mounted specimen, the PPC specimen, or the floating specimen.

Our finding that PC stretch depends on specimen dimensions will affect these comparisons and further exacerbate known differences in mechanics between reference configurations (Laurence et al. (2022)).

Finally, our results demonstrate that the use of different specimen dimensions in experimental characterizations does not have a significant effect on the estimated constitutive model parameters. The only significant difference was the Tong-Fung constitutive model parameter (c) between different sizes of TVPL and TVSL. Therefore, we have shown that the considered experimental parameters of the commercial BioTester device do not significantly affect the estimated parameters of the constituive model for use in *in silico* simulations.

4.4. Study Limitations and Future Extensions

There are several limitations in this study. First, the specimens were taken from the biaxial tester between tests on specimens of different sizes. This likely resulted in inconsistent, stress-free mounted configurations that could affect our comparisons. An additional control group may have helped to understand these effects, but we expect only a minimal influence on our results since the tests were performed after preconditioning, at approximate *in vivo* forces and considering fiducial markers within the central 70% of the effective test region (see also the Supplementary Material). Interestingly, our unpublished preliminary data suggest that tissue swelling may play a more important role in the long-term mechanical characterization of the TV leaflets and will be explored in future investigations. Second, we used *rigid* tines to mount the tissues to the biaxial testing device that limits possible shear deformation of the tissue. A previous study by Fehervary et al. (2016) demonstrated that this mounting scheme is suitable for characterizing the *biaxial tensile* properties of soft tissues. Third, the number/distribution of BioRake tines and apron dimensions were different for each specimen size in the present investigation. The computational study of Fehervary et al. (2016) showed that the apron dimensions do not have a significant influence on the experimental characterizations, whereas a uniform distribution of tines was critical to ensure strain homogeneity. On the other hand, Eilaghi et al. (2009) came up with conflicting findings, stating that the number of tines is critical to ensure homogeneous strains. The *in silico* investigations contained in the Supplementary Material to this article showed that the mounting configurations used in the associated experiments should not have a significant affect on the interpretation of our results. Finally, the constitutive modeling did not consider the average mechanical response for each specimen size. This was intentional to test whether the specimen dimensions affect specimen-specific model parameters. Due to the highly nonlinear nature of the constitutive models, the median model parameters should not be used to represent the average size-specific behavior Khoiy et al. (2018).

In addition, there are several potential extensions of this investigation. For example, the experimental protocol could be modified to account for a dense speckle pattern. This would allow the determination of a refined strain field that could be analyzed to understand how specimen dimensions alter strain heterogeneity within the test region. This was partially done in a recent study by Dover et al. (2022) in which the authors used polarized spatial frequency domain imaging with 10×10 mm bovine pericardial specimens and determined

that edge effects were minimal within the central 8 × 8 mm, which was similar to the central 70% region found in our *in silico* studies shown in the Supplementary Material. A second extension of this work could focus on the large number of data from existing TV biomechanics studies (Table 4) to see if the observed (or missing) trends are confirmed for a larger number of samples and other specimen dimensions. We have attempted to capture the range of specimen dimensions in the existing literature, but existing studies often use specimen dimensions within that range appropriate to their investigation and purpose.

4.5. Conclusion

This study provided the first experimental investigation of how specimen dimensions affect the mechanical behavior, mechanical properties, and constitutive model parameters obtained from biaxial tensile characterizations. It was found that smaller specimen dimensions generally exhibited a stiffer circumferential behavior and a more compliant radial behavior, although the differences were not statistically significant. Furthermore, the derived mechanical properties were also affected by specimen dimensions, with the low-tensile modulus increasing, the high-tensile modulus decreasing, and the anisotropy index increasing as specimen dimensions became smaller. Finally, the equibiaxial tension data were fitted with three constitutive models used for soft biological tissues. Interestingly, for the Tong-Fung constitutive model, we found only one significant difference between two specimen sizes of TVPL and TVSL. This underscores that the choice of specimen dimensions in experimental characterizations does not necessarily play an important role in the development of computational models of heart valves that utilize the experimental mechanical data.

Supplementary Material

Refer to Web version on PubMed Central for supplementary material.

Acknowledgments.

We thank the funding support from the American Heart Association Scientist Development Grant (16SDG27760143), the Presbyterian Health Foundation, and the NIH NHLBI R01 (HL159475). DWL was supported in part by the American Heart Association/Children Heart Foundation Predoctoral Fellowship #821298 and the National Science Foundation Graduate Research Fellowship (2019254233). SW acknowledges the support of the National Science Foundation CAREER Award CMMI-1847062.

Appendix A: Results for the Non-Equibiaxial Protocols

The mechanical behavior of all three TV leaflets under non-equibiaxial protocols (i.e., $f_{\text{circ}}^{\max}:f_{\text{rad}}^{\max}=1:0.667,1:0.333,0.667:1,0.333:1$) are presented in this Appendix, i.e., Figs. A.1–A.4.

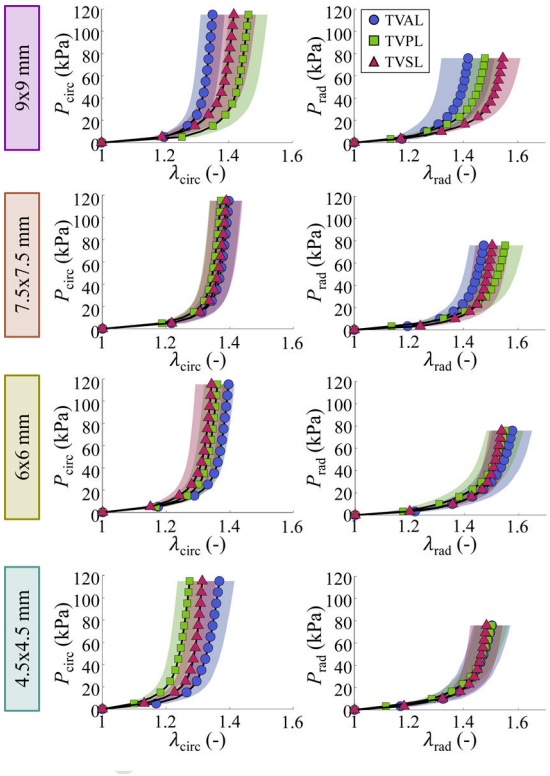

Figure A1:

Mechanical behavior for biaxial tensions ($P_{circ} : P_{rad} = 1 : 0.667$) of the three TV leaflets represented as mean (solid curves) ± standard error of the mean. $P_{(\bullet)}$ and $\lambda_{(\bullet)}$ denote the first Piola-Kirchhoff stress and the stretch, respectively. TVAL: TV anterior leaflet, TVPL: TV posterior leaflet, and TVSL: TV septal leaflet.

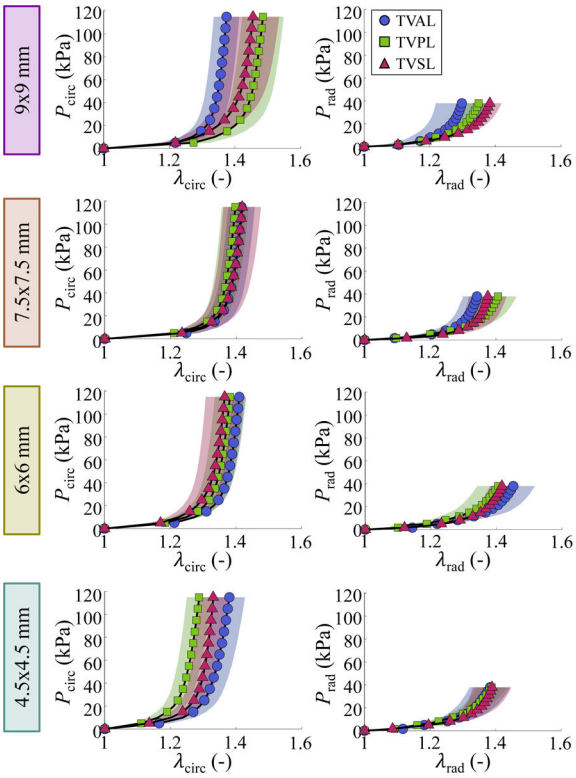

Figure A2:

Mechanical behavior for biaxial tensions (P_{circ} : P_{rad} = 1 : 0.333) of the three TV leaflets represented as mean (solid curves) ± standard error of the mean. $P_{(\bullet)}$ and $\lambda_{(\bullet)}$ denote the first Piola-Kirchhoff stress and the stretch, respectively. TVAL: TV anterior leaflet, TVPL: TV posterior leaflet, and TVSL: TV septal leaflet.

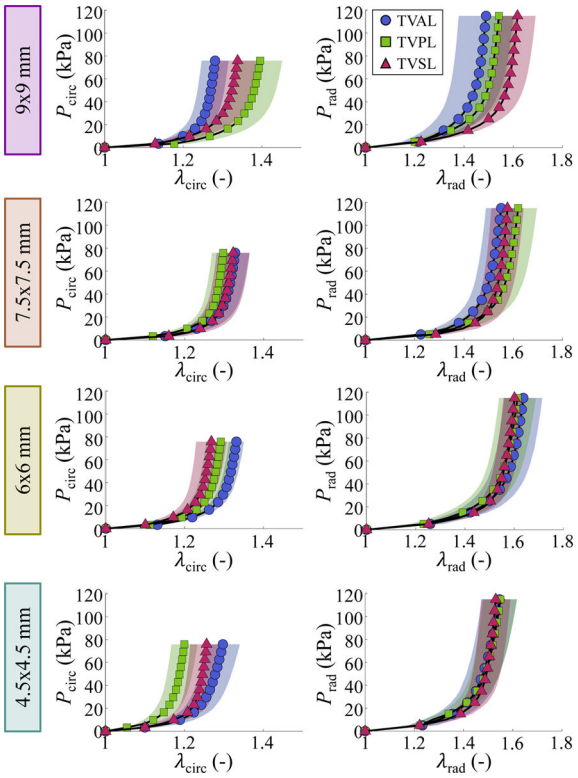

Figure A3:

Mechanical behavior for biaxial tensions (P_{circ} : P_{rad} = 0.667 : 1) of the three TV leaflets represented as mean (solid curves) ± standard error of the mean. $P_{(\bullet)}$ and $\lambda_{(\bullet)}$ denote the first Piola-Kirchhoff stress and the stretch, respectively. TVAL: TV anterior leaflet, TVPL: TV posterior leaflet, and TVSL: TV septal leaflet.

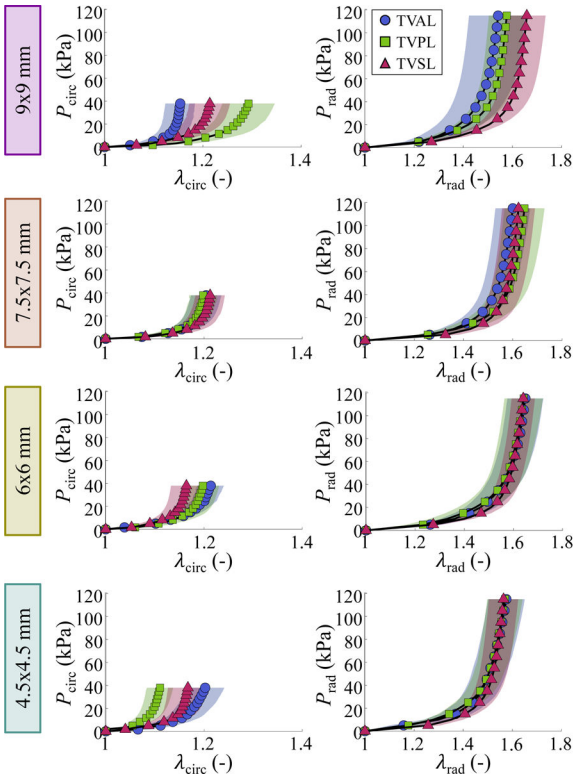

Figure A4:

Mechanical behavior for biaxial tensions ($P_{circ} : P_{rad} = 0.333 : 1$) of the three TV leaflets represented as mean (solid curves) ± standard error of the mean. $P_{(\bullet)}$ and $\lambda_{(\bullet)}$ denote the first Piola-Kirchhoff stress and the stretch, respectively. TVAL: TV anterior leaflet, TVPL: TV posterior leaflet, and TVSL: TV septal leaflet.

References

Avanzini A, Battini D, 2016. Integrated experimental and numerical comparison of different approaches for planar biaxial testing of a hyperelastic material. Advances in Materials Science and Engineering 2016. doi:10.1155/2016/6014129.

Clarin J, Dang D, Santos L, Amini R, 2023. Mechanical characterization of porcine tricuspid valve anterior leaflets over time: Applications to ex vivo studies. ASME Open Journal of Engineering 2, 021032. doi:10.1115/1.4062477.

Dover CM, Goth W, Goodbrake C, Tunnell JW, Sacks MS, 2022. Simultaneous wide-field planar strain–fiber orientation distribution measurement using polarized spatial domain imaging. Annals of Biomedical Engineering 50, 253–277. doi:10.1007/s10439-021-02889-7. [PubMed: 35084627]

Duginski GA, Ross CJ, Laurence DW, Johns CH, Lee CH, 2020. An investigation of the effect of freezing storage on the biaxial mechanical properties of excised porcine tricuspid valve anterior leaflets. Journal of the Mechanical Behavior of Biomedical Materials 101, 103438. doi:10.1016/j.jmbbm.2019.103438. [PubMed: 31542570]

Eilaghi A, Flanagan JG, Brodland GW, Ethier CR, 2009. Strain uniformity in biaxial specimens is highly sensitive to attachment details. Journal of Biomechanical Engineering 131. doi:10.1115/1.3148467.

Fehervary H, Smoljkić M, Vander Sloten J, Famaey N, 2016. Planar biaxial testing of soft biological tissue using rakes: A critical analysis of protocol and fitting process. Journal of the Mechanical Behavior of Biomedical Materials 61, 135–151. doi:10.1016/j.jmbbm.2016.01.011. [PubMed: 26854936]

Gasser TC, Ogden RW, Holzapfel GA, 2006. Hyperelastic modelling of arterial layers with distributed collagen fibre orientations. Journal of the Royal Society Interface 3, 15–35. doi:10.1098/rsif.2005.0073. [PubMed: 16849214]

Holzapfel GA, 2000. Nonlinear Solid Mechanics. A Continuum Approach for Engineering. John Wiley & Sons, Chichester.

Hudson LT, Jett SV, Kramer KE, Laurence DW, Ross CJ, Towner RA, Baumwart R, Lim KM, Mir A, Burkhart HM, et al. , 2020. A pilot study on linking tissue mechanics with load-dependent collagen microstructures in porcine tricuspid valve leaflets. Bioengineering 7, 60. doi:10.3390/bioengineering7020060. [PubMed: 32570939]

Jacobs NT, Cortes DH, Vresilovic EJ, Elliott DM, 2013. Biaxial tension of fibrous tissue: using finite element methods to address experimental challenges arising from boundary conditions and anisotropy. Journal of Biomechanical Engineering 135. doi:10.1115/1.4023503.

Jett SV, Hudson LT, Baumwart R, Bohnstedt BN, Mir A, et al. , 2020. Integration of polarized spatial frequency domain imaging (pSFDI) with a biaxial mechanical testing system for quantification of load-dependent collagen architecture in soft collagenous tissues. Acta Biomaterialia 102, 149–68. doi:10.1016/j.actbio.2019.11.028. [PubMed: 31734412]

Jett SV, Laurence DW, Kunkel RP, Babu AR, Kramer KE, et al. , 2018. An investigation of the anisotropic mechanical properties and anatomical structure of porcine atrioventricular heart valves. Journal of the Mechanical Behavior of Biomedical Materials 87, 155–71. doi:10.1016/j.jmbbm.2018.07.024. [PubMed: 30071486]

Khoiy KA, Amini R, 2016. On the biaxial mechanical response of porcine tricuspid valve leaflets. Journal of Biomechanical Engineering 138, 104504. doi:10.1115/1.4034426.

Khoiy KA, Pant AD, Amini R, 2018. Quantification of material constants for a phenomenological constitutive model of porcine tricuspid valve leaflets for simulation applications. Journal of Biomechanical Engineering 140, 094503. doi:10.1115/1.4040126.

Kramer KE, Ross CJ, Laurence DW, Babu AR, Wu Y, Towner RA, Mir A, Burkhart HM, Holzapfel GA, Lee CH, 2019. An investigation of layer-specific tissue biomechanics of porcine atrioventricular valve anterior leaflets. Acta Biomaterialia 96, 368–384. doi:10.1016/j.actbio.2019.06.049. [PubMed: 31260822]

Laurence DW, Ross CJ, Hsu MC, Mir A, Burkhart HM, Holzapfel GA, Lee CH, 2022. Benchtop characterization of the tricuspid valve leaflet pre-strains. Acta Biomaterialia 152, 321–334. [PubMed: 36041649]

Laurence DW, Ross CJ, Jett SV, Johns CH, Echols A, Baumwart R, Towner R, Liao J, Bajona P, Wu Y, Lee CH, 2019. An investigation of regional variations in the biaxial mechanical properties and stress relaxation behaviors of porcine atrioventricular heart valve leaflets. Journal of Biomechanics 83, 16–27. doi:10.1016/j.jbiomech.2018.11.015. [PubMed: 30497683]

Lee CH, Amini R, Gorman RC, Gorman III JH, Sacks MS, 2014. An inverse modeling approach for stress estimation in mitral valve anterior leaflet valvuloplasty for in-vivo valvular biomaterial assessment. Journal of Biomechanics 47, 2055–2063. [PubMed: 24275434]

May-Newman K, Yin FC, 1995. Biaxial mechanical behavior of excised porcine mitral valve leaflets. American Journal of Physiology Heart and Circulatory Physiology 269, H1319–27. doi:10.1152/ajpheart.1995.269.4.H1319.

Meador WD, Mathur M, Sugerman GP, Jazwiec T, Malinowski M, Bersi MR, Timek TA, Rausch MK, 2020a. A detailed mechanical and microstructural analysis of ovine tricuspid valve leaflets. Acta Biomaterialia 102, 100–113. doi:10.1016/j.actbio.2019.11.039. [PubMed: 31760220]

Meador WD, Mathur M, Sugerman GP, Malinowski M, Jazwiec T, Wang X, Lacerda CM, Timek TA, Rausch MK, 2020b. The tricuspid valve also maladapts as shown in sheep with biventricular heart failure. Elife 9, e63855. doi:10.7554/eLife.63855. [PubMed: 33320094]

Narang H, Rego BV, Khalighi AH, Aly A, Pouch AM, Gorman RC, Gorman III JH, Sacks MS, 2021. Pre-surgical prediction of ischemic mitral regurgitation recurrence using in vivo mitral valve leaflet strains. Annals of biomedical engineering, 1–13. [PubMed: 32691263]

Nielsen P, Hunter P, Smaill B, 1991. Biaxial testing of membrane biomaterials: Testing equipment and procedures. Journal of Biomechanical Engineering 113. doi:10.1115/1.2894887.

Nolan D, McGarry J, 2016. On the correct interpretation of measured force and calculation of material stress in biaxial tests. Journal of the Mechanical Behavior of Biomedical Materials 53, 187–199. [PubMed: 26327453]

Pham T, Sulejmani F, Shin E, Wang D, Sun W, 2017. Quantification and comparison of the mechanical properties of four human cardiac valves. Acta Biomaterialia 54, 345–55. doi:10.1016/j.actbio.2017.03.026. [PubMed: 28336153]

Pokutta-Paskaleva A, Sulejmani F, DelRocini M, Sun W, 2019. Comparative mechanical, morphological, and microstructural characterization of porcine mitral and tricuspid leaflets and chordae tendineae. Acta Biomaterialia 85, 241–252. doi:10.1016/j.actbio.2018.12.029. [PubMed: 30579963]

Ross C, Laurence D, Wu Y, Lee CH, 2019a. Biaxial mechanical characterizations of atrioventricular heart valves. Journal of Visualized Experiments, e59170 doi:10.3791/59170.

Ross CJ, Laurence DW, Echols AL, Babu AR, Gu T, Duginski GA, Johns CH, Mullins BT, Casey KM, Laurence KA, et al. , 2021. Effects of enzyme-based removal of collagen and elastin constituents on the biaxial mechanical responses of porcine atrioventricular heart valve anterior leaflets. Acta Biomaterialia 135, 425–440. doi:10.1016/j.actbio.2021.08.043. [PubMed: 34481053]

Ross CJ, Laurence DW, Richardson J, Babu AR, Evans LE, Beyer EG, Childers RC, Wu Y, Towner RA, Fung KM, et al. , 2019b. An investigation of the glycosaminoglycan contribution to biaxial mechanical behaviours of porcine atrioventricular heart valve leaflets. Journal of the Royal Society Interface 16, 20190069. doi:10.1098/rsif.2019.0069. [PubMed: 31266416]

Sacks MS, 2000. Biaxial mechanical evaluation of planar biological materials. Journal of Elasticity and the Physical Science of Solids 61, 199–246. doi:10.1023/A:1010917028671.

Sacks MS, Drach A, Lee CH, Khalighi AH, Rego BV, Zhang W, Ayoub S, Yoganathan AP, Gorman RC, Gorman III JH, 2019. On the simulation of mitral valve function in health, disease, and treatment. Journal of Biomechanical Engineering 141, 070804.

Salinas SD, Clark MM, Amini R, 2019. Mechanical response changes in porcine tricuspid valve anterior leaflet under osmotic-induced swelling. Bioengineering 6, 70. doi:10.3390/bioengineering6030070. [PubMed: 31443151]

Salinas SD, Clark MM, Amini R, 2020. The effects of −80°C short-term storage on the mechanical response of tricuspid valve leaflets. Journal of Biomechanics 98, 109462. doi:10.1016/j.jbiomech.2019.109462. [PubMed: 31718820]

Salinas SD, Farra YM, Amini Khoiy K, Houston J, Lee CH, Bellini C, Amini R, 2022. The role of elastin on the mechanical properties of the anterior leaflet in porcine tricuspid valves. Plos one 17, e0267131. doi:10.1371/journal.pone.0267131. [PubMed: 35560311]

Sugerman G, Yang J, Rausch M, 2023. A speckling technique for dic on ultra-soft, highly hydrated materials. Experimental Mechanics, 1–6 doi:10.1007/s11340-023-00938-x.

Sun W, Sacks MS, Scott MJ, 2005. Effects of boundary conditions on the estimation of the planar biaxial mechanical properties of soft tissues. Journal of Biomechanical Engineering 127. doi:10.1115/1.1933931.

Tong P, Fung YC, 1976. The stress-strain relationship for the skin. Journal of Biomechanics 9, 649–657. doi:10.1016/0021-9290(76)90107-X. [PubMed: 965417]

Wells SM, Pierlot CM, Moeller AD, 2012. Physiological remodeling of the mitral valve during pregnancy. American Journal of Physiology-Heart and Circulatory Physiology 303, H878–H892. doi:10.1152/ajpheart.00845.2011. [PubMed: 22886410]

Wobbrock JO, Findlater L, Gergle D, Higgins JJ, 2011. The aligned rank transform for nonparametric factorial analyses using only anova procedures, in: Proceedings of the SIGCHI Conference on Human Factors in Computing Systems, pp. 143–146. doi:10.1145/1978942.1978963.

Yu WJ, Shen M, Chen WN, Zhan ZH, Gong YJ, Lin Y, Liu O, Zhang J, 2014. Differential evolution with two-level parameter adaptation. IEEE Transactions on Cybernetics 44, 1080–1099. doi:10.1109/TCYB.2013.2279211. [PubMed: 24013834]

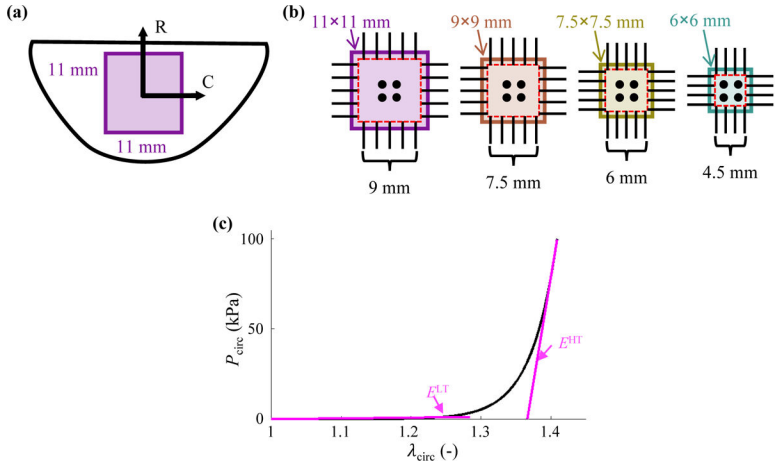

Figure 1:

(a) Central region of the tricuspid valve leaflet was prepared and (b) mounted to the commercial biaxial tester for an iterative approach to determine the effect of specimen sizes on the observed mechanical properties. (Red dashed lines denote the effective tissue region of each specimen size.) (c) Determination of the low-tensile moduli E^{LT} and the high-tensile moduli E^{HT} for a representative tissue direction. (P_{circ} and λ_{circ} denote the first Piola-Kirchhoff stress and the stretch in the circumferential direction, respectively.)

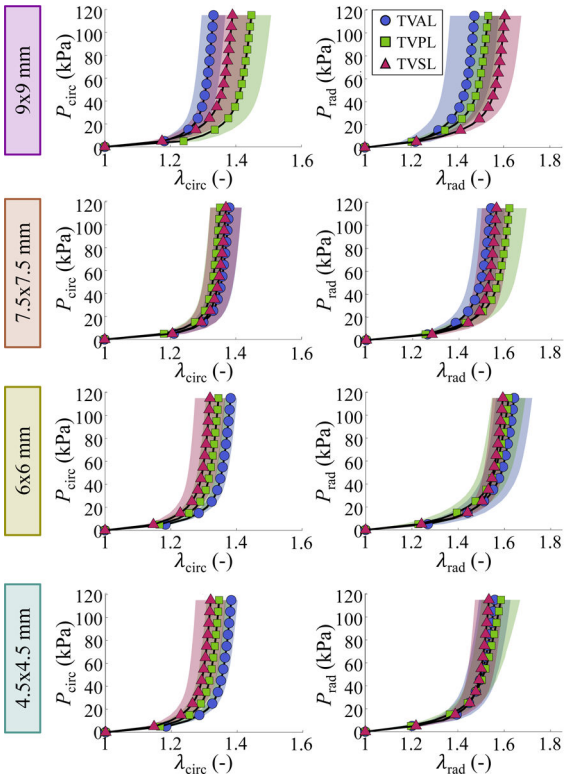

Figure 2:

Mechanical behavior for equibiaxial tensions (P_{circ} : P_{rad} = 1 : 1) of the three TV leaflets represented as mean (solid curves) ± standard error of the mean (shaded areas). $P_{(\bullet)}$ and $\lambda_{(\bullet)}$ denote the first Piola-Kirchhoff stress and tissue stretch, respectively. TVAL: TV anterior leaflet, TVPL: TV posterior leaflet, and TVSL: TV septal leaflet.

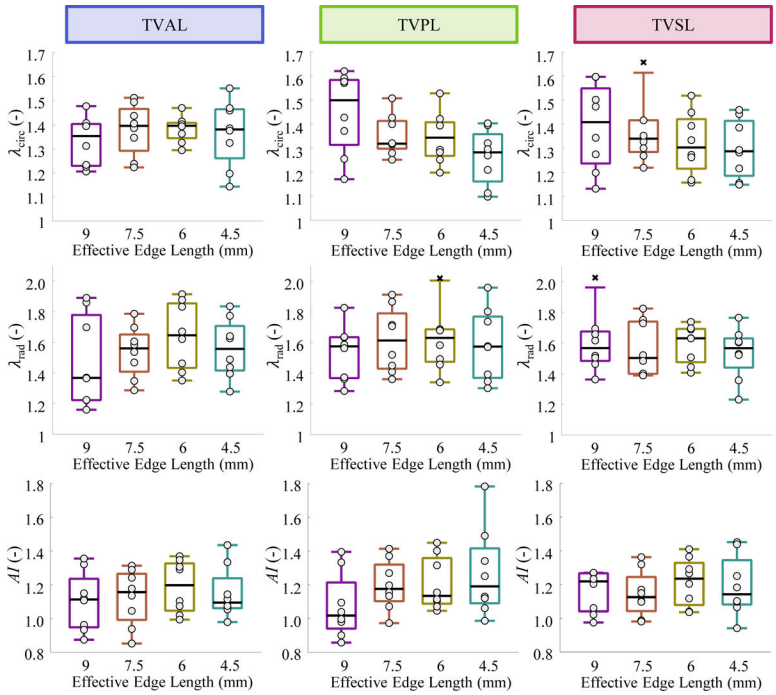

Figure 3:

(*Top*) Peak circumferential stretch, (*middle*) peak radial stretch and (*bottom*) anisotropy index (*AI*) for the four specimen sizes of all three TV leaflets. × denotes outliers, $\lambda_{(\bullet)}$ denotes the stretch, TVAL: TV anterior leaflet, TVPL: TV posterior leaflet, and TVSL: TV septal leaflet.

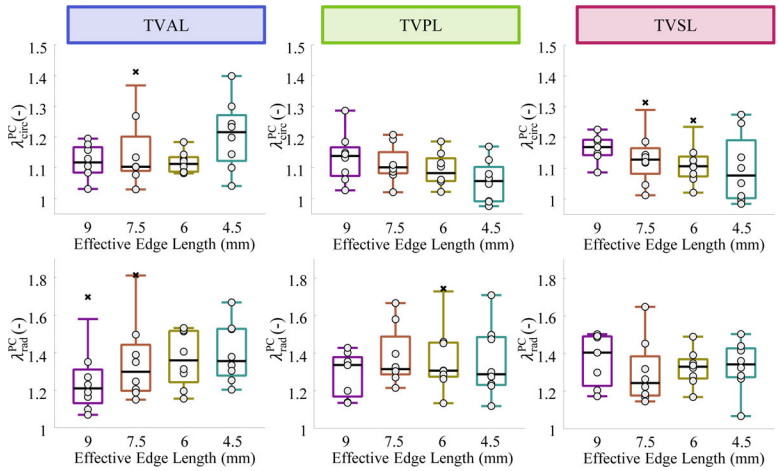

Figure 4:

Preconditioning stretches for the four specimen sizes of all three TV leaflets in (*top*) circumferential and (*bottom*) radial directions, where × denotes an outlier; $\lambda_{(\bullet)}^{PC}$ denotes the quantified stretches after the preconditioning step. TVAL: TV anterior leaflet, TVPL: TV posterior leaflet, and TVSL: TV septal leaflet.

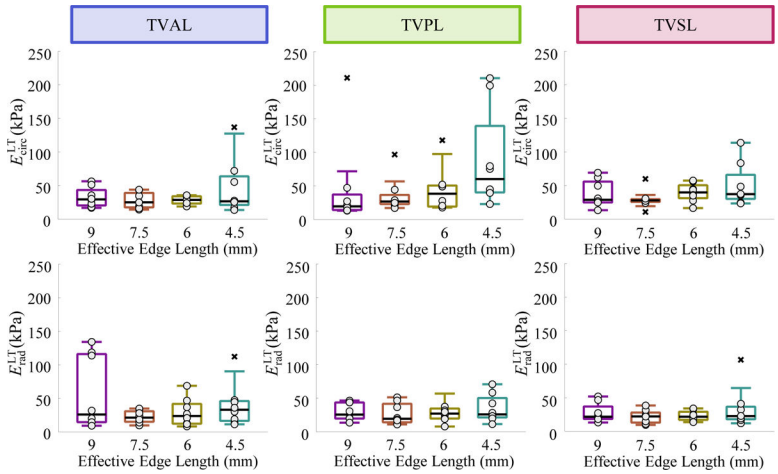

Figure 5:

Low-tensile moduli (E_{circ}^{LT} and E_{rad}^{LT}) for the four specimen sizes of all three TV leaflets in (*top*) circumferential and (*bottom*) radial directions, where × denotes an outlier. TVAL: TV anterior leaflet, TVPL: TV posterior leaflet, and TVSL: TV septal leaflet.

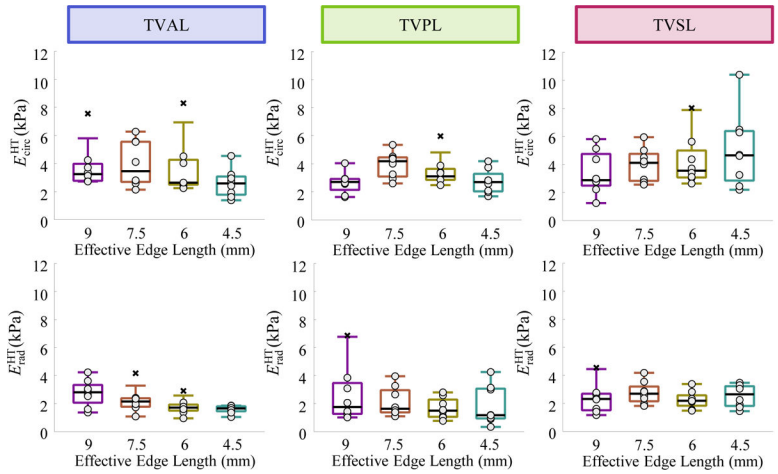

Figure 6:

High-tensile moduli (E_{circ}^{HT} and E_{rad}^{HT}) for the four specimen sizes of all three TV leaflets in (*top*) circumferential and (*bottom*) radial directions, where × denotes an outlier. TVAL: TV anterior leaflet, TVPL: TV posterior leaflet, and TVSL: TV septal leaflet.

Table 1:

Estimated parameters for the Lee-Sacks model, i.e., Eq. (3), fitted to the equibiaxial mechanical response of all three tricuspid valve leaflets.

Parameter	Leaflet	Size 1			Size 2			Size 3			Size 4			p-value		
		Median	1st	3rd	Median	1st	3rd	Median	1st	3rd	Median	1st	3rd	Leaflet	Size	Interaction
c_0 (kPa)	AL	0.45	0.06	3.03	0.29	0.06	0.66	0.22	0.01	2.52	1.03	0.04	6.57	0.56	0.14	0.21
	PL	0.35	0.09	4.15	0.23	0.03	0.66	1.32	0.11	5.66	3.45	0.73	4.09			
	SL	0.34	0.08	0.57	0.03	0.02	0.30	0.26	0.04	0.72	0.15	0.01	1.67			
c_1 (kPa)	AL	2.82	1.00	6.28	1.86	1.12	2.79	1.58	1.00	2.36	1.44	1.07	2.30	0.06	0.22	0.17
	PL	1.15	1.00	2.02	1.31	1.00	2.71	1.00	1.00	1.88	1.05	1.00	1.90			
	SL	1.20	1.00	2.13	2.52	1.98	3.19	1.29	1.15	1.83	1.61	1.00	2.57			
c_2 (–)	AL	6.92	2.90	13.92	6.31	3.72	15.53	5.65	2.42	7.17	4.16	3.42	6.37	0.20	0.38	0.21
	PL	3.29	2.62	11.73	5.02	3.34	9.25	2.55	2.20	6.25	2.50	1.57	6.42			
	SL	3.26	1.21	9.44	6.87	4.76	8.55	4.27	3.29	6.31	7.26	6.02	15.40			
δ (–)	AL	0.00	0.00	0.06	0.00	0.00	0.28	0.00	0.00	0.49	0.00	0.00	0.41	0.89	0.73	0.83
	PL	0.00	0.00	0.30	0.00	0.00	0.42	0.00	0.00	0.01	0.00	0.00	0.00			
	SL	0.00	0.00	0.61	0.00	0.00	0.49	0.00	0.00	0.00	0.00	0.00	0.26			
θ (deg.)	AL	44.14	41.01	46.27	41.33	20.18	45.40	39.71	19.50	41.71	43.10	19.73	43.99	0.78	0.95	0.86
	PL	45.11	31.53	47.25	40.55	38.70	42.11	40.80	37.48	43.35	39.37	36.06	42.87			
	SL	40.75	29.56	42.38	42.08	25.82	44.17	40.11	38.89	42.34	42.35	36.89	43.17			

The data presented include the median, first quartile (1^{st}), and third quartile (3^{rd}). AL: anterior leaflet, PL: posterior leaflet, and SL: septal leaflet.

Table 2:

Estimated parameters for the Tong-Fung model, i.e., Eq. (4), fitted to the equibiaxial mechanical response of all three tricuspid valve leaflets.

Parameter	Leaflet	Size 1			Size 2			Size 3			Size 4			p-value		
		Median	1st	3rd	Median	1st	3rd	Median	1st	3rd	Median	1st	3rd	Leaflet	Size	Interaction
c (kPa)	AL	0.29	0.08	0.80	0.21	0.02	0.64	0.28	0.02	1.94	0.73	0.14	2.01	<0.01	<0.01	0.16
	PL	0.32	0.15	1.22	0.16	0.02	0.49	0.91	0.15	2.87	0.86*	0.44	3.04			
	SL	0.34	0.14	0.50	0.04*	0.02	0.14	0.17	0.05	0.25	0.14	0.02	0.58			
a_1 (−)	AL	4.30	1.45	6.03	3.28	0.96	5.40	1.72	0.29	3.27	2.85	0.42	6.47	0.78	0.94	0.90
	PL	0.76	0.07	2.98	2.34	0.54	7.78	2.28	0.08	5.12	2.59	0.21	7.40			
	SL	2.19	0.60	20.58	1.85	0.00	11.40	1.91	0.10	14.76	0.66	0.00	11.60			
a_2 (kPa)	AL	3.28	1.90	6.01	1.74	0.39	3.75	1.78	0.94	2.99	1.67	0.87	3.77	0.33	0.94	0.29
	PL	0.21	0.02	1.85	1.96	1.41	4.11	1.67	0.92	2.78	1.66	1.08	5.78			
	SL	1.65	0.71	5.50	2.97	1.42	4.84	2.27	1.61	3.32	2.66	1.82	3.59			
a_3 (kPa)	AL	9.74	1.63	15.60	3.89	2.38	7.14	2.92	1.67	3.92	3.13	1.10	5.51	0.43	0.44	0.33
	PL	3.81	3.00	5.24	2.57	0.68	10.51	2.51	1.25	5.81	2.71	0.81	5.10			
	SL	2.03	0.64	3.90	5.14	1.64	7.18	4.65	1.99	6.05	7.03	2.99	9.19			

The data presented include the median, first quartile (1st), and third quartile (3rd). AL: anterior leaflet, PL: posterior leaflet, SL: septal leaflet, and * denotes statistically significant pairwise comparison.

Table 3:

Estimated parameters for the Gasser-Ogden-Holzapfel (GOH) model, i.e., Eq. (5), fitted to the equibiaxial mechanical response of all three tricuspid valve leaflets.

Parameter	Leaflet	Size 1			Size 2			Size 3			Size 4			p-value		
		Median	1st	3rd	Median	1st	3rd	Median	1st	3rd	Median	1st	3rd	Leaflet	Size	Interaction
k_1 (kPa)	AL	0.46	0.08	74.49	0.45	0.06	3.33	0.22	0.04	24.15	11.05	0.08	42.16	0.20	0.36	0.89
	PL	0.40	0.09	17.69	0.86	0.03	9.72	8.18	0.12	18.39	15.58	1.66	49.86			
	SL	0.49	0.12	2.80	0.09	0.04	8.78	0.30	0.07	1.02	0.97	0.03	3.74			
k_2 (−)	AL	14.29	2.87	37.92	6.33	4.86	8.69	5.31	2.73	9.42	5.76	3.42	10.49	0.24	0.34	0.58
	PL	7.26	2.62	12.52	5.30	3.09	19.27	6.15	3.67	7.01	5.72	3.01	10.25			
	SL	4.74	3.26	7.50	6.87	5.08	13.29	5.40	3.84	9.53	7.55	6.11	11.36			
κ (–)	AL	0.00	0.00	0.25	0.00	0.00	0.14	0.00	0.00	0.31	0.00	0.00	0.30	0.31	0.81	0.83
	PL	0.00	0.00	0.28	0.00	0.00	0.30	0.00	0.00	0.28	0.17	0.00	0.28			
	SL	0.00	0.00	0.19	0.00	0.00	0.16	0.00	0.00	0.00	0.00	0.00	0.25			
θ (deg.)	AL	42.95	39.28	47.59	41.24	26.77	45.40	39.44	19.16	44.21	42.86	19.72	43.68	0.69	0.29	0.74
	PL	45.11	37.36	46.54	39.07	0.38	42.11	39.47	0.00	43.72	19.10	0.00	43.14			
	SL	40.59	29.88	42.78	42.59	39.13	44.36	40.11	38.89	42.34	41.22	35.03	42.38			

The data presented include the median, first quartile (1st), and third quartile (3rd). AL: anterior leaflet, PL: posterior leaflet, and SL:septal leaflet.

Table 4:

Existing investigations in the literature characterizing the mechanical properties of the tricuspid heart valve leaflets.

PI	Paper	Dissected Dimensions	Mounted Dimensions	Stress Measure	Deformation Measure
Chung-Hao Lee	Jett et al. (2018)	8 mm	6.5 mm	1PK	Stretch
	Laurence et al. (2019)	6 mm	4 mm	MT	Stretch
	Ross et al. (2019b)	10 mm	7/5.5 mm	MT	Stretch
	Kramer et al. (2019)	4 mm	3.5 mm	1PK	Stretch
	Duginski et al. (2020)	10 mm	6.5–8.5 mm	MT	Stretch
	Hudson et al. (2020)	ND	10 mm	MT	Stretch
	Ross et al. (2021)	10 mm	7.5/6 mm	MT	Stretch
Manuel Rausch	Meador et al. (2020a)	7 mm	ND	MT	Stretch
	Meador et al. (2020b)	7 mm	ND	MT	Stretch
Rouzbeh Amini	Khoiy and Amini (2016)	11 mm	7.6 mm	MT	Stretch
	Salinas et al. (2022)	11 mm	7.6 mm	1PK	Green Strain
	Salinas et al. (2019)	11 mm	7.6 mm	1PK	Green Strain
	Clarin et al. (2023)	11 mm	7.6 mm	1PK	Green Strain
	Salinas et al. (2020)	11 mm	7.6 mm	1PK	Green Strain
Wei Sun	Pokutta-Paskaleva et al. (2019)	ND	ND	2PK	Green Strain
	Pham et al. (2017)	ND	10 mm	2PK	Green Strain

(ND: Not Defined, 1PK: First Piola-Kirchhoff, MT: Membrane Tension, 2PK: Second Piola-Kirchhoff)